Published in final edited form as:

IEEE Sens J. 2017 ; 17(22): 7394–7404. doi:10.1109/JSEN.2017.2760140.

Real-Time *In Vivo* Intraocular Pressure Monitoring using an Optomechanical Implant and an Artificial Neural Network

Kun ho Kim,
Department of Computer Science, California Institute of Technology, Pasadena, CA 91125 USA

Jeong Oen Lee,
Department of Electrical Engineering and the Department of Medical Engineering, California Institute of Technology, Pasadena, CA 91125 USA

Juan Du,
Department of Ophthalmology, University of California, San Francisco CA 94143 USA

David Sretavan, and
Department of Ophthalmology, University of California, San Francisco CA 94143 USA

Hyuck Choo
Department of Electrical Engineering and the Department of Medical Engineering, California Institute of Technology, Pasadena, CA 91125 USA

Abstract

Optimized glaucoma therapy requires frequent monitoring and timely lowering of elevated intraocular pressure (IOP). A recently developed microscale IOP-monitoring implant, when illuminated with broadband light, reflects a pressure-dependent optical spectrum that is captured and converted to measure IOP. However, its accuracy is limited by background noise and the difficulty of modeling non-linear shifts of the spectra with respect to pressure changes. Using an end-to-end calibration system to train an artificial neural network (ANN) for signal demodulation we improved the speed and accuracy of pressure measurements obtained with an optically probed IOP-monitoring implant and make it suitable for real-time in vivo IOP monitoring. The ANN converts captured optical spectra into corresponding IOP levels. We achieved an IOP-measurement accuracy of ±0.1 mmHg at a measurement rate of 100 Hz, which represents a ten-fold improvement from previously reported values. This technique allowed real-time tracking of artificially induced sub-1 s transient IOP elevations and minor fluctuations induced by the respiratory motion of the rabbits during in vivo monitoring. All in vivo sensor readings paralleled those obtained concurrently using a commercial tonometer and showed consistency within ±2 mmHg. Real-time processing is highly useful for IOP monitoring in clinical settings and home environments and improves the overall practicality of the optical IOP-monitoring approach.

Correspondence to: Hyuck Choo.

Index Terms

Glaucoma; intraocular pressure; implant; in vivo; optical sensing; biomedical signal processing; neural network

I. Introduction

Glaucoma refers to a class of eye conditions that cause gradual and irreversible optic nerve damage, which eventually leads to vision loss. By 2020, 76 million people worldwide will be affected by the disease; 4.5 million will suffer irreversible bilateral vision loss [1], [2]. Though the pathophysiology of glaucoma is poorly understood, elevated intraocular pressure (IOP) stands to be the singular modifiable risk factor for open-angle glaucoma. Currently, the only available therapeutic modalities are moderating elevated IOP levels by administering medication and performing surgical procedures [3]. Because IOP is known to fluctuate over the course of the day [4], [5], it is difficult for clinicians to optimize glaucoma therapy based on sparse IOP measurements taken at the clinic several times a year [6], [7]. Thus, there is a need for home-based IOP-monitoring systems [8].

Generally, home-based IOP monitoring technologies need to satisfy the following requirements: (1) *IOP-measurement accuracy better than* ±2 mmHg, a clinically accepted accuracy range [9]; and (2) a *high sampling rate* and *real-time processing* to shorten measurement time and improve the practicality of the sensing approach [10], [11]. Fast, accurate, and convenient IOP measurements would also allow surgeons to monitor and countermeasure acute IOP spikes more effectively during the immediate postoperative period and to prevent optic nerve damage [12], [13]. Furthermore, high-speed and high-frequency IOP monitoring could elucidate the pathophysiology of glaucoma and reveal new diagnostic and therapeutic possibilities. Several studies have reported using a temporal frequency analysis of IOP pulses as a promipsing method of diagnosing glaucoma [14], [15]. Low-amplitude (< 4 mmHg) oscillatory IOP pulses (> 4 Hz) synchronized with the cardiac system have also been correlated with normal-tension glaucoma [16], [17], which is very common in Japan. However, most widely used clinic-based tonometers are incapable of providing high-speed, accurate IOP measurements. They must also be operated by trained personnel, so frequent measurements at home are not possible.

A contact-based dynamic contour tonometer (DCT) with ±1 mmHg readout accuracy at a 100-Hz sampling rate was used in a clinical setting to obtain continuous IOP measurements [18]. Recently explored sensor-based IOP-monitoring technologies [19–26] include wireless LC implants [27] with accuracy of 2.5 mmHg, implantable micro-fluidic channel sensors [28] with 0.5-mmHg sensitivity, and soft-contact lens strain gauges [29] that provide relative IOP profiling in voltage readouts at 10 Hz. A summary of the state-of-the-art IOP sensing technologies is provided in Table I. These technologies have shown promise for further miniaturization and improvement.

We previously reported the development of a biocompatible IOP-sensing implant that measured less than 0.9 mm in diameter and provided remote optical readout (Fig. 1(a)) [30], [31]. Our IOP sensor is a hermetically sealed optical resonant cavity made of a flexible

silicon nitride (SiN) membrane on the top and a rigid silicon surface on the bottom with the internal pressure at 1 atm (Fig. 1(b)) [31].

When the sensor is interrogated by near-infrared (NIR) region (790–1150 nm) of a broadband light source such as a tungsten light bulb, the sensor reflects an optical resonance spectrum (Fig. 1(d)) which is captured using an optical scope connected to a spectrometer. The captured spectrum is relayed to a computer for analysis. A decrease or increase in ambient pressure deforms the flexible membrane, which changes the gap size between the top and bottom surfaces and consequently the optical resonance of the cavity (Fig. 1(c)). As a result, every optical resonance uniquely maps to a particular ambient pressure (Fig. 1(d)) [31]. The donut-shaped peripheral area of the top surface outside the SiN membrane is covered with black silicon which effectively suppresses undesired background reflection, increases the sensor readout distance to 12 cm, and improves biocompatibility (the right inset of Fig. 1(a)). [30]

A change in ambient pressure shifts the sensor's resonant spectrum as shown in Fig. 1(c–d) or more specifically the locations of the valleys that belong to the spectrum as illustrated in Fig. 1(d). To utilize this sensor for accurate, real-time IOP readouts, we must first learn a mapping between the optical spectra (Fig. 1(d)) and the corresponding pressure. Fig. 1(e) plots the valley locations vs. IOP, and each line presents the location of an individual valley as a function of ambient pressure. Then, during the actual measurement, a captured spectrum can be processed by a signal-demodulation algorithm (SDA) and converted to the corresponding IOP value. How accurately and quickly the SDA accomplishes the spectrum to IOP mapping plays an important role in determining the sensor's final sensitivity and sampling rate.

Mapping between an optical signal and the corresponding IOP is a complex, nonlinear procedure because of background noise and disappearance of key spectral features, mainly valleys, from the spectrometer's measurement range as the pressure increases or decreases. Valleys disappearing out of the measurement window are shown along the left edge of the plot in Fig. 1(d). For example, the first valley λ_1 in Fig. 1(d) is visible only from 1 to 2 mmHg and disappears from the measurement range of the spectrometer as the pressure continues to increase. Hence to make a continuous linear approximation to map IOP over the full 0–30 mmHg range used to require manually combining all the lines shown in Fig. 1(e). However, such manual stitching created discontinuities or jumps at the vanishing valley points in the line of sensor IOP measurement vs. digital pressure gauge readout (Fig. 1(f)), resulting in a large readout inaccuracy. Previously, using manual post-processing, we obtained a readout accuracy of ±1 mmHg [30], [31]. We were not able to produce real-time measurements.

Here we report an application of an artificial neural network (ANN) to IOP signal demodulation and demonstrate improved IOP readouts with ±0.1 mmHg accuracy at a 100-Hz measurement rate in the clinically relevant pressure range of 0–30 mmHg (Fig. 1(g)). ANNs are universal function-approximators that have been used successfully to solve non-linear mapping problems in the field of biomedical signal processing [32–37].

Application of an ANN-based SDA to IOP-sensor signal processing with implementation of an end-to-end ANN training system allowed us to develop a highly accurate and fast IOP measurement system that could track transient IOP elevations. We also evaluated the performance of the IOP sensor by carrying out accuracy and temporal frequency analysis on measurements obtained experimentally in *in vitro* and *in vivo* experiments. The results we report in this paper exceed the performance metrics of the aforementioned sensing technologies and satisfy the requirements for home-based IOP monitoring technologies. The outcomes suggest that the remote optical IOP-sensing approach has potential for further development into a reliable home IOP-monitoring system for glaucoma patients and drug-discovery research.

II. Methodology

An increase in ambient pressure corresponds to the blue-shifted spectrum, while a decrease in pressure corresponds to a red shift. Because the sensor's optical reflection is uniquely determined by the ambient pressure, IOP can be obtained by demodulating the reflection spectrum. The locations of the resonant spectrum minima provide crucial information for signal demodulation, as they are uniquely determined by the extent of membrane deflection. By tracing the valleys while altering the ambient pressure, we can simplify the complicated behavior of the spectrum shift with a lower dimensional representation, which is plotted in Fig. 1(e). The insets of Fig. 1(d) demonstrate the gradual process of how the leftmost valley *vanishes*. Because of this *vanishing valley effect*, it is difficult to make a linear fit to the spectrum shift without introducing significant mapping errors. Hence, in the clinically relevant 0–30 mmHg range, the mapping between valley locations and corresponding IOP becomes non-linear, thus posing a major challenge in demodulation.

In the past, ANNs have been applied to non-linear signal demodulation in a variety of fields including medical engineering [32–37] and speech recognition [38]. In particular, they have been shown to outperform other non-linear function approximators (i.e. support vector machines and tree based estimators) for regression problems (with that said, other function approximators may also perform moderately well for this problem). Inspired by previous successful implementations, we applied ANN regression to our problem of demodulating an optical signal reflected from the IOP-sensing implant to discover the non-linear mapping between the optical spectra and the corresponding IOP. The valley locations and spacing between adjacent valleys are fed into a trained ANN which outputs IOP as shown in Fig. 1(g). The expressivity of ANNs allow us to accurately map the valley locations, which are fairly robust against background noise, to IOP instead of having to process the entire signal. In this methods section, we describe in detail (1) the automated ANN training process, (2) *in vitro* performance test procedures, and (3) *in vivo* experimental procedures for rabbit eye measurements.

A. ANN Training on an Optical Bench

The overall ANN training and implementation flow is presented in Fig. 2. A pressure-controlling data-acquisition system was designed to automatically generate training sets for the ANN. This set-up is shown in Fig. 3(a). Our system integrates an optical detector

(consisting of a microscope, spectrometer, charge-coupled device [CCD] camera, and light source), a pressurized fluid chamber with a mechanical system to induce step changes in pressure, and an electronic pressure sensor with a data acquisition (DAQ) board. The spectrometer and DAQ board were connected to a main computer (Macbook Air, 1.6 GHz Intel Core i5, 8GB RAM, 1600 MHz DDR3 memory, Apple, CA, USA), which processed the data to generate training sets for the ANN.

For optical measurements, we placed the IOP sensor inside a pressurized chamber and collected light reflected from the sensor using an optical scope. We used a custom-built microscope integrated with an objective lens (20×, Plan, Apo, Infinity Corrected, Long Working Distance, Mitutotyo, Kawasaki, Japan), a USB camera (STC-MB133USB, Sentech Co., Atsugi, Japan), a broadband light source (Ocean Optics HL-2000, Dunedin, FL, USA), and a commercially available VIS-NIR spectrometer (MAYA 2000 Pro, Ocean Optics, Dunedin, FL, USA) with wavelength range of 780–1200 nm, spectral resolution of 0.22 nm, and minimum integration time of 9 ms.

While the optical reflection was measured, the pressure inside the chamber was monitored using a commercial digital pressure gauge (1210, TE Connectivity, USA) with accuracy of ±0.1 mmHg. The mV output of the digital pressure gauge was amplified by two stage operational amplifiers and relayed to a microcontroller (Arduino Uno, Arduino, Somerville, MA, USA) that allows ms-resolution monitoring of reference pressure inside the chamber. To systematically vary the chamber pressure in the full range of 0–30 mmHg, a programmable syringe pump was used (NE 1000, ABC Scientific, CA, USA).

While varying the pressure, the spectrometer and reference digital pressure gauge were simultaneously triggered for a readout from the main computer every 10 ms. The main computer then recorded the outputs. After generating a unit training set composed of 40,000 recordings, the raw spectrum data were passed through a moving average low-pass filter to smooth the signal with a span of 20 data points and then onto the valley-detection function, which extracted the dip locations. As the *input*s to the training set, we chose (1) the two leftmost extracted valley locations (($\lambda_{\mathbf{n}}$ and $\lambda_{\mathbf{n+1}}$ in Fig. 1(g))) at the time of measurement; and (2) the distances between the left-most and the second left-most valleys ($\Delta\lambda_{\mathbf{n,n+1}}$ in Fig. 1(e), (g)) and also between the second left-most and the third left-most valleys ($\Delta\lambda_{\mathbf{n,n+1}}$ in Fig. 1(g)). The reference-pressure values from the digital gauge were also passed through a low-pass filter to attenuate the high-frequency noise and then recorded as the *target predictions* (or labels) of the training set. The reason for including inter-valley spacing as a feature is described in section III-A. Our automated training system generates a unit training set in less than 7 min by recording and processing 40,000 spectra. A full training set for the ANN consists of two such unit sets (80,000 spectra).

Due to the inherent variations in microfabrication processes, each microfabricated sensor has slightly different dimensions that lead to different mechanical properties (or pressure vs. membrane deflection in our case) and consequently different resonance profiles. Hence, we must generate a new training set for every new sensor and retrain the ANN. The weights of the trained ANN are stored in a sensor characteristics database and retrieved later for signal demodulation of the particular sensor.

The calibration of a sensor could also be dependent on the optical emission profile of the light source. Hence, if necessary, we can pre-characterize the emission profile of a light source and remove it from the measured data. However, we used the same light source throughout our experiments, and captured spectra with strong resonant signals and low background noises. Hence, recalibration was not necessary, and the influence of the emission profile of the light source on IOP measurements was minimal.

B. Performance Characterizations in a Pressure-Controlled Chamber

We characterized on an optical bench the accuracy and measurement rate of our sensor integrated with the ANN-based SDA. To test the pressure resolution and repeatability in the full 0–30 mmHg pressure span, we utilized the same pressure-controlled chamber used for training the ANN. The SDA-processed sensor outputs and the reference pressure gauge values were recorded simultaneously while linearly varying the pressure at a rate of 0.03 mmHg/s, up to 30 mmHg. We then evaluated the temporal resolution of our SDA by performing high-frequency pressure-fluctuation tests. A high-precision mechanical oscillator (U56001, 3B Scientific, USA) programmed with a function generator was used to feed sinusoidal pressure fluctuations into the test chamber while the SDA-processed sensor output and the reference digital pressure gauge values were recorded. Fast Fourier Transform (FFT) analysis was performed on the time-series pressure data to evaluate the accuracy of frequency detection, which would indicate the suitability of using our system for temporal frequency analysis of an IOP pulse or detection of fast transient IOP changes.

C. Performance Tests In Vivo

In order to obtain real-time measurements of IOP *in vivo*, we performed IOP measurements on anesthetized New Zealand white rabbits obtained from Western Oregon Rabbit Company (Philomath, OR USA). The corneas in these rabbits are widely known to closely resemble those of a human [39], [40]. The rabbit subjects were housed in a facility at University of California San Francisco (UCSF) approved by the United States Department of Agriculture. All uses of animals in this work adhered to the Association for Research in Vision & Ophthalmology Statement for the Use of Animals in Ophthalmic and Vision Research. The experimental protocols were approved by the Institutional Animal Care and Use Committee (IACUC) of the UCSF.

Fig. 3(b) and 3(c) show the *in vivo* experimental set-up, with an anesthetized rabbit undergoing spectrum measurements. We collected data from a sensor that had been implanted in the rabbit eye for 9 months without any sign of deterioration in functionality. The IOP sensor was characterized before implantation. In order to achieve fast, accurate *in vivo* IOP monitoring of live rabbit eyes, we performed rapid intravitreal injections. Next, 5% hypertonic saline was injected into the rabbit eye to trigger an acute IOP elevation, which caused the rabbit's IOP to spike from 16 mmHg to approximately 25 mmHg. IOP was measured from the implant at a rate of 100 Hz. Recordings were obtained during multiple, sequential 1-minute sessions during the intravitreal injection. Intermittent baseline IOP measurements were obtained using a commercial tonometer for animals with accuracy of ±2 mmHg (TonoVet, Icare, Vanda, Finland). Temporal frequency analysis was performed for

short-term measurements. The *in vivo* optical readout setup was identical to the set-up used for *in vitro* characterization of the sensor.

To obtain proper resonance spectra from the reflection, the current version of the IOP sensor requires perpendicular optical alignment between the implanted device and the optical readout system. Processing corrupted signals arising from misalignments of the set-up can yield erroneous IOP values. *In vivo* measurements are more prone to misalignment because of movements of the rabbit eye and respiratory motions. Correct optical alignment must be achieved in three orientations (transverse, longitudinal, and angular) in order to obtain proper resonance spectra. First, the light probe should be fixated at a transverse coordinate within a valid focal range to prevent saturated or insufficient reflection. Second, probing light should be focused on or near the center of the sensors' diaphragm to minimize peripheral reflections from the cavity contour. Finally, the incident angle of probing light hitting the sensor surface should be within 10 degrees. Angular misalignment of 10 degrees can increase the measurement error up to ±2 mmHg which is within the clinically accepted error range [9]. Beyond 10 degrees, the signal-to-noise ratio of the resonance spectra becomes too low and undetectable. Such spectra are filtered out by a misalignment-recognition module integrated in the valley-detection module for *in vivo* signal processing. (see bottom of Fig. 2)

The impact of misalignment induced errors and signal filtering are mitigated by the fast measurement rate of 100 Hz which allows us to average out around 100 IOP values per second. Hence, even if 90 % of the measured data is invalid, we can still obtain an accurate IOP value using the other 10 valid spectra. The validity of this approach has been confirmed by an established IOP-sensing device TonoVet during *in vivo* studies [30], [31]. For future improvement, we are currently developing an omnidirectional sensor whose resonance is incident-angle-invariant. Moreover, an automated alignment device and a handheld detector are under development to allow easy convenient tracking of the sensor to improve the practicality of the IOP sensing approach.

III. Results & Discussion

A. Model Parameters and Input Feature Selection

The ANN comprised two hidden layers each with 11 neurons activated by a rectified linear unit (ReLU) non-linearity. The network weights were regularized using the $L2$-norm of the weights ($L2$-regularized, $C = 0.0001$) to improve generalization. Mean squared error was used as the loss for training. A computationally inexpensive architecture, which can be trained in seconds without GPUs, was sufficient to achieve excellent out-of-sample performance, as shown in section III-B. This shows that the chosen input-feature vector is robust and informative. The optimal number of neurons was found using 10-fold cross-validation, with which we evaluated the dependence of estimated test accuracy on the number of hidden units. The results plotted in Fig. 4 demonstrate that the mean cross-validation error reaches and stays close to the minimum value after 11 neurons.

As mentioned earlier, the input-feature vector comprised (1) the locations of the two leftmost valleys and (2) the inter-valley spacing associated with them. Because valleys

occasionally disappear before reaching the left edge of the spectrometer's measurement range, we set a hard threshold (840nm) for the minimum detection wavelength. To verify the benefit of including the inter-valley spacing in the input to the ANN, we conducted network training with and without the inter-valley spacing parameter and saw great improvement in calibration accuracy when spacing was included, reducing the average validation error from 1.27×10^{-2} mmHg to 6.24×10^{-5} mmHg which is about 3 orders of magnitude lower. Hence, we have concluded that spacing is a critical parameter that aids the learning algorithm in converging to a local minimum closer to the global minimum in the feature space. Choosing the valley location and inter-valley spacing as input features made the ANN more robust against background noise and variations in optical conditions during *in vivo* measurements. This approach allowed us to focus on the specific attributes of the resonance spectrum instead of processing it in its entirety and to reduce the number of regression predictors and thus the associated computation time.

The bottom 3D plot in Fig. 5 shows IOP plotted against the location of the leftmost valley and its distance to the right adjacent valley. The top left and right plots show 2D projections of the 3D plot, IOP vs left-most valley location and IOP vs valley spacing, respectively. From this, we can infer that a legitimate feature vector has been constructed, because one-to-one mapping is observed between the combined input space (of the valley location and inter-valley spacing) and the corresponding IOP values. We train the network with a mini-batch size of 100 using the Adam optimizer [41] with $\alpha = 0.001$, $\beta_1 = 0.9$ and $\beta_2 = 0.999$. On average, training took 52.5 seconds and 550 epochs to converge. A trained ANN took an average of 50.58 μs to process a new spectrum and convert it to a measurement of IOP.

A forward pass through ANN (which is essentially a series of matrix multiplications) with a computationally inexpensive architecture can easily be implemented in miniaturized computational devices, such as smartphones and Raspberry Pi, which have less processing power. A computation-efficient algorithm compatible with a miniaturized computational platform is critical for implementing a more compact and practical readout system. Further miniaturization of the overall readout system in a compact head mount is a current work in progress.

B. Pressure Detection Range and Sensitivity

The ANN was trained to perform within a clinically relevant physiologically observed IOP range of 0–30 mmHg. To test the sensor's sensitivity in the full detection range, we compared the pressure response of the IOP sensor with the readings from the reference digital pressure gauge while linearly varying the pressure from 1 mmHg to 30 mmHg (see Fig. 6(a)). A subsection of the plot from 8 to 9 mmHg was magnified in Fig. 6(b) and shows a very close agreement between the sensor readout and the reference pressure line. The mean squared error between the output of the ANN function and that of the reference pressure gauge was 6.24×10^{-5} mmHg. Moreover, by performing a correlation analysis on the outputs from the ANN and the reference pressure sensor, we found the correlation coefficient R to be close to 1 ($1 - R = 2.15\times10^{-6}$) and the p-value to be close to 0. The repeatability of the IOP sensor was measured to be 0.043% FS (0.013 mmHg), with no sign of hysteresis. Considering these miniscule statistical error values, we concluded that the

ANN is capable of a pressure-readout accuracy equivalent to that of the reference digital pressure gauge (i.e. ±0.1 mmHg).

During the ANN calibration, the reference pressure sensor sensitivity limited the overall accuracy of the ANN to ±0.1 mmHg, which still exceeds the accuracy reported for preceding sensor-based IOP monitoring technologies (±0.5 mmHg was the highest achieved by [28]) and clinic-based measurement techniques (±1 mmHg achieved by DCT [18]). Furthermore, this result shows a ten-fold improvement in accuracy from our previous opto-mechanics-based SDA [30] which achieved ±1 mmHg accuracy. We expect the sensor accuracy to further improve if we use a more precise reference pressure gauge. High accuracy is critical for characterizing low-amplitude components of an IOP pulse such as the ocular pulse amplitude, which have been correlated with glaucoma [17]. The development of convenient and reliable IOP measurement tools with high accuracy will widen the field of glaucoma research, as will be further described in section III-D.

C. Transient Pressure Fluctuation Detection

High temporal resolution IOP readout could be a critical attribute of an IOP-monitoring system. It is necessary to perform temporal frequency analysis of a patient's IOP pulse and to track transient IOP spikes that could damage the optic nerve. Most clinically relevant information of a patient's IOP profile can be extracted by capturing daily periodic IOP fluctuations as well as the influence of the respiratory and cardiac pulses which oscillate below 10 Hz. Hence, we first show that the ocular implant is capable of precisely capturing pressure fluctuations at the upper bound of 10 Hz, with a capability to resolve small incremental changes in the frequency of applied pressure.

Fig. 7(a) displays the pressure readout from the IOP sensor compared with the reference pressure from the digital gauge in response to a sinusoidal pressure fluctuation, applied at a frequency of 10 Hz. The data present a close match between the SDA-processed sensor output and the reference-gauge values, both of which resemble sinusoidal waveforms. The FFT of the time-series IOP data (see Fig. 7(b)) reveals a sharp peak at 10 Hz, indicating that the SDA-processed pressure readout reproduced the waveform which is almost perfectly sinusoidal with negligible amount of noise. From this result, we can infer that our IOP-sensing system properly captured both the frequency and waveform of the applied fluctuation.

Next, the sensitivity of the IOP sensor's response to incremental changes in the frequency of pressure fluctuation was assessed by FFT analysis. The peak frequency in the FFT spectrum of the time-series IOP data was compared to the applied frequency. The applied frequency was fine-tuned in 0.05-Hz increments from 10 Hz to 10.95 Hz. The plot that compares the measured frequency and the applied frequency is shown in Fig. 7(c). The mean squared error between the measured and applied frequencies was 5.25×10^{-6} Hz, and a linear correlation test yielded $R = 0.997$ and $p = 8.61 \times 10^{-155}$. These results show that our sensor combined with the ANN-based SDA can accurately detect temporal frequency components in fluctuating IOP, suggesting our system can be used to extract periodic IOP pulses with clinical value.

To test the temporal frequency-detection limit of our system for measuring fast pressure fluctuations, we measured the response of the system in 5-Hz increments up to 50 Hz. We observed sharp, distinct FFT peaks at each of the pressure fluctuation frequencies applied to the system, up to 50 Hz. At driving frequencies beyond 50 Hz, one Fourier resonance peak at the applied frequency as well as another peak mirrored at about 50 Hz was identified. This cutoff phenomenon can be quantitatively explained with the Nyquist frequency, which is the half of the sampling frequency. Because the sampling rate was 100 Hz, the Nyquist frequency of our detection system was 50 Hz, which matched the experimental observations.

The spectrometer integration time of 9 ms was the limiting factor placing an upper bound on the pressure measurement rate because the execution time of the ANN-based SDA was only about 50 μs. Using a higher-quality spectrometer with a more light-sensitive detector and shorter integration time, our system could detect IOPs at a much faster rate, possibly up to 5000 Hz.

The frequency-detection experiments described above were conducted with medium-amplitude (approximately 4 mmHg) fluctuations in pressure. Next, to verify the capability of our system in detecting acute high-amplitude fluctuations in IOP, we emulated a single high-amplitude (approximately 20 mmHg) IOP spike, which is believed to damage the optic nerve [42]. We induced a 20-mmHg pressure spike using a syringe pump and compared the sensor measurements with the pressure values obtained using the reference digital gauge. Fig. 7(d) shows close agreement between the reference pressure-gauge readout and the SDA-processed sensor output (MSE: 8.3×10^{-5}mmHg), which validates the ability of our detection system (hardware and software) to properly track IOP fluctuations ranging from small periodic pulses to sporadically occurring fast, high-amplitude spikes.

D. IOP Monitoring In Vivo

Here, we present *in vivo* IOP monitoring results obtained by demodulating the reflection spectra from our IOP-sensing implant, which had been surgically placed inside the anterior chamber of the rabbit. Fast IOP-tracking capability was verified through a saline-injection test (see Fig. 8(a)). IOP values obtained prior to the injection were measured as approximately 17 mmHg and 16 mmHg with the IOP-sensing implant and the Tonovet, respectively. Four minutes after the intravitreal injection, the rabbit's IOP surged by 4 mmHg and peaked during the following 30-s period. Because of the high-readout speed enabled by the ANN-based SDA, we were able to track this transient change in IOP during the 30-s period while the conventional Tonovet was not able to detect it. The maximum IOP reached approximately 24.5 mmHg. The peak lasted for approximately 1 minute, and after that, IOP began to decline. After 15 minutes, both the IOP sensor and the Tonovet readings were close to approximately 17 mmHg, which indicated that IOP had decreased to the baseline level. Both the implanted sensor readings and Tonovet measurements showed good consistency and traced the elevation and reduction in IOP.

Our rapid SDA also allowed us to visualize subtle fluctuation patterns in IOP that could not be observed in Tonovet measurements. As shown in Fig. 8(b), the respiration of the rabbit caused 1.5-mmHg pseudo-periodic dips in IOP measurements. Fig. 8(c) shows the FFT of the time-series IOP data shown in Fig. 8(b). The temporal frequency peak of the measured

IOP data at 0.42 Hz matched the lower end of the normal respiratory rate (0.5–1 Hz) in rabbits. This result is in agreement with the fact that anesthetized rabbits typically have lower breathing rates. The respiratory rate that was independently measured using a breathing-rate monitor (Hallowell EMC Model 2000, Hallowell EMC, MA, USA) was 0.43 Hz, which differed by only 0.01 Hz from the primary temporal frequency peak shown in Fig. 8(c). Inhalation caused a transient decrease in IOP, which quickly rebounded to its original levels upon exhalation [43]. This phenomenon occurs because inhalation causes transient surges in venous return, which temporarily facilitates aqueous humor drainage, causing transient dips in the IOP pulse. As most IOP tracking systems generate discrete measurements at a lower pressure resolution, such respiratory pulses have not been observed, and thus measurements obtained using such systems may underestimate the true IOP. A rapid IOP monitoring system allows measurements averaged over a shorter, selected time interval to filter out the transient IOP changes induced by respiration.

Being able to monitor the respiratory rate by tracking IOP not only expands the number of clinically relevant quantities that are being measured but also significantly lowers the error rate of IOP measurements. Studies have shown that a frequent source of IOP-measurement error is breath holding [44]. Breath holding frequently occurs during clinic measurements when the patient gets anxious. Such changes are difficult to detect without monitoring the respiratory rate, which is difficult to achieve using conventional IOP-sensing technologies. An IOP monitoring system capable of continuous real-time readout can concurrently track the respiratory rate of patients and detect breath holding to produce more accurate IOP values.

Aside from IOP fluctuations that synchronize with the respiratory system, certain temporal features of the cardiac IOP pulses have high clinical utility, such as the Ocular Pulse Amplitude (OPA), which is considered valuable information [45] for glaucoma management and diagnosis [16], [17]. However, the cardiac IOP pulses exhibit low amplitudes (< 4 mmHg) and high frequencies (> 4 Hz), suggesting only monitoring systems that are sufficiently accurate and fast can provide these parameters with high clinical value. For example, numerical values of higher harmonics observed in the FFT analysis of an IOP pulse can be used to discriminate between patients with glaucoma and healthy subjects [14], [15], but such measurements cannot be performed using current tonometric methods. The *in vivo* transient IOP-tracking ability demonstrated in Fig. 8 along with the *in vitro* experiment results of Figs. 6 and 7 suggest that our system could be the first sensor-based IOP-monitoring technology that could allow researchers to explore in detail the clinical value of the temporal frequency features of an IOP pulse. Using our system's SDA-enabled fast measurement capability, we are in the process of further investigating such temporal frequency features of IOP pulses for clinical utilities.

IV. Conclusion

In this work, we have investigated a light-probed IOP sensor's potential for fast and reliable IOP readouts, which would ultimately contribute to glaucoma research and management. When using an ANN-based SDA, the IOP sensors' accuracy and measurement rate were ±0.1 mmHg and 100 Hz, respectively, in *in vitro* testing. Combined use of our sensor with

the ANN-based SDA allowed us to obtain highly accurate and detailed IOP profile from live rabbits. This result demonstrates the feasibility of using our sensing approach to perform temporal frequency analysis of an IOP pulse and to retrieve highly valued clinical information. The reliable performance of our sensing approach has great potential for further development into a convenient home-based IOP-measurement system: patients can take periodic measurements throughout the day, and any abnormality can be automatically reported to a clinician in a timely manner. Such systems may even allow monitoring of IOP during, for example, a physically intensive routine, such as a gym work-out, to elucidate the correlation between physical activity and surges in IOP levels. We are continuing our effort to develop a user-friendly IOP-monitoring system; this algorithm takes us many steps closer to the implementation of a highly practical and portable IOP-monitoring system.

Acknowledgments

The authors would like to extend a special thanks to Yisong Yue at the California Institute of Technology for discussions on the algorithm design. We also thank William Kettyle, and Nauman Javed at the Harvard School of Medicine for helpful discussions on the influence of respiration on IOP levels. We also thank the veterinarians at the UCSF ophthalmology department for assisting our experiments. This research has been funded by the National Institute of Health, the Heritage Medical Research Foundation, and the Caltech Innovation program.

The project was funded by the National Institute of Health (NIH) EY024582, HMRI Investigator Award, and donations of Fredrick W. Drury under a research fellowship program at the California Institute of Technology.

Biographies

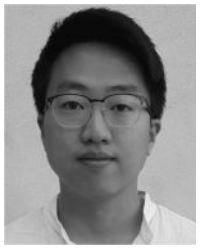

Kun ho Kim is pursuing the B.S. degree in computer science at the California Institute of Technology in Pasadena, CA. He is expected to graduate in 2018. He was a summer undergraduate research fellow at the California Institute of Technology in 2016 and at Stanford University in 2017.

His research interests range from advancing theoretical understandings of reinforcement learning to developing practical applications of machine learning algorithms in various real-world domains. Recent research topics include developing policy search methods for coordinating multiple agents, applying machine learning techniques to quantify bipedal standing performance of patients with spinal cord injuries, and designing embedding networks for crowd-based image labeling systems.

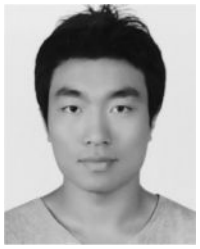

Jeong Oen Lee received the B.S. degree, the M.S. degree, and the Ph.D. degree in Electrical Engineering from KAIST (Daejeon, South Korea). Since 2013, he has been working as a post-doctoral researcher in Electrical Engineering and Medical Engineering at California Institute of Technology (CA, USA).

His current research interests and activities are focused on translational medical-engineering research. The specific topics include applications of micro-/nanoscale devices in biomedical sensing and development of implantable sensors and monitoring systems.

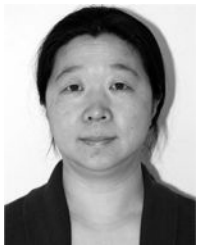

Juan Du received the M.D. degree and M.S degree from Norman Bethune University of Medical Sciences in China in 1995; she received the Ph.D. degree from Peking University in 2001. She received residency training in the Department of Ophthalmology in the First Hospital, Norman Bethune University of Medical Sciences from 1995 to 1998. She Worked in Sretavan Lab in UC San Francisco as a postdoctoral research fellow since 2002, and she is currently an associate specialist in the lab.

Her other area of work includes exploring the mechanisms of retinal ganglion cells degeneration in the diseases of glaucoma.

David Sretavan received the B.Sc. degree in Physiology from McGill University (Montreal, Canada) and the M.D. degree and the Ph.D. degree in Neuroscience from Stanford University (Stanford, CA. USA). He joined the Departments of Ophthalmology and

Physiology at the University of California in San Francisco in 1994 where he is currently Professor of Ophthalmology and Vice-Chair for Research.

His areas of research interest include axonal injuries, optic neuropathies, glaucoma, and advanced technologies that impact diagnostic as well as treatment paradigms for ocular and other conditions.

Hyuck Choo received the B.S. degree and the M. Eng. degree in electrical engineering from Cornell University in Ithaca, NY and the Ph.D. degree in electrical engineering and computer sciences (EECS) from the UC Berkeley, where he also completed postdoctoral training in conjunction with the UC San Francisco. Since 2011, he has been an assistant professor in Electrical Engineering and Medical Engineering at the California Institute of Technology.

His research focuses on utilizing micro-/nanoscience and electrical engineering to develop innovative medical technologies that will enable breakthrough discoveries and also bring about cost-effective solutions to major medical problems such as glaucoma, diabetes, and atherosclerosis.

Nomenclature

Adam	Adaptive moment estimation
α	Learning rate for the Adam optimizer
ANN	Artificial neural network
β_1	1st moment decay rate for the Adam optimizer
β_2	2nd moment decay rate for the Adam optimizer
C	L2 regularization constant
DCT	Dynamic contour tonometer
FFT	Fast Fourier transform
FS	Full span
IOP	Intraocular pressure
λ_n	Location of the n^{th} valley in the measurement range

$\Delta\lambda_{n,n-1}$	Spectral spacing between the n^{th} and $(n-1)^{th}$ valley
MSE	Mean squared error
NIR	Near-infrared
OPA	Ocular pulse amplitude
p	*p*-value (calculated probability)
SDA	Signal demodulation algorithm
SiN	Silicon nitride
R	Pearson product-moment correlation coefficient

References

1. Quigley HA, Broman AT. The number of people with glaucoma worldwide in 2010 and 2020. Br J Ophthalmol. 2006; 90(3):262–267. [PubMed: 16488940]
2. Tham YC, et al. Global prevalence of glaucoma and projections of glaucoma burden through 2040: a systematic review and meta-analysis. Ophthalmology. 2014; 121(11):2081–2090. [PubMed: 24974815]
3. Coleman AL. Advances in glaucoma treatment and management: surgery. Invest Ophthalmol Vis Sci. 2012; 53(5):2491–2494. [PubMed: 22562849]
4. Klein BE, et al. Intraocular pressure in an American community. The Beaver Dam Eye Study. Invest Ophthalmol Vis Sci. 1992; 33(7):2224–2228. [PubMed: 1607232]
5. Agnifili L, et al. Circadian intraocular pressure patterns in healthy subjects, primary open angle and normal tension glaucoma patients with a contact lens sensor. Acta Ophthalmol. 2015; 93(1):14–21.
6. Hughes E, et al. 24-hour monitoring of intraocular pressure in glaucoma management: a retrospective review. J Glaucoma. 2003; 12(3):232–236. [PubMed: 12782841]
7. Mansouri K, et al. Analysis of continuous 24-hour intraocular pressure patterns in glaucoma. Invest Ophthalmol Vis Sci. 2012; 53(13):8050–8056. [PubMed: 23139273]
8. Mosaed S, et al. Correlation between office and peak nocturnal intraocular pressures in healthy subjects and glaucoma patients. Am J Ophthalmol. 2005; 139(2):320–324. [PubMed: 15733994]
9. Bengtsson B, et al. Fluctuation of intraocular pressure and glaucoma progression in the early manifest glaucoma trial. Ophthalmology. 2007; 114(2):205–209. [PubMed: 17097736]
10. Bui BV, et al. The gradient of retinal functional changes during acute intraocular pressure elevation. Invest Ophthalmol Vis Sci. 2005; 46(1):202–213. [PubMed: 15623775]
11. Strouthidis NG, et al. Effect of acute intraocular pressure elevation on the monkey optic nerve head as detected by spectral domain optical coherence tomography. Invest Ophthalmol Vis Sci. 2011; 52(13):9431–9437. [PubMed: 22058335]
12. Gross JG, et al. Increased intraocular pressure in the immediate postoperative period after extracapsular cataract extraction. Am J Ophthalmol. 1988; 105(5):466–469. [PubMed: 3369515]
13. Shingleton BJ, et al. Evaluation of intraocular pressure in the immediate period after phacoemulsification. J Cataract Refract Surg. 2011; 27(4):524–527.
14. Evans DW, et al. Spectral content of the intraocular pressure pulse wave: glaucoma patients versus normal subjects. Graefes Arch Clin Exp Ophthalmol. 2002; 240(6):475–480. [PubMed: 12107515]
15. Widlicka M, et al. Clinical utility of spectral analysis of intraocular pressure pulse wave. BMC Ophthalmol. 2014; 14(1):30. [PubMed: 24620786]
16. Schwenn O, et al. Ocular pulse amplitude in patients with open angle glaucoma, normal tension glaucoma, and ocular hypertension. Br J Ophthalmol. 2002; 86(9):981–984. [PubMed: 12185121]
17. Sturmer JP, Kniestedt C. Role of ocular pulse amplitude in glaucoma. Klin Monbl Augenheilkd. 2015; 232(2):162–168. [PubMed: 25700254]

18. Hoffmann EM, et al. Intraocular pressure and ocular pulse amplitude using dynamic contour tonometry and contact lens tonometry. BMC Ophthalmol. 2004; 4(1):4. [PubMed: 15038831]
19. Chitnis G, et al. A minimally invasive implantable wireless pressure sensor for continuous IOP monitoring. IEEE Trans Biomed Eng. Jan.2013 60(1)
20. Chen GZ, et al. Capacitive contact lens sensor for continuous noninvasive intraocular pressure monitoring. Sens Actuators A: Phys. 2013; 203:112–118.
21. Mansouri K, et al. Continuous intraocular pressure monitoring with a wireless ocular telemetry sensor: initial clinical experience in patients with open angle glaucoma. Br J Ophthalmol. 2011; bjo-2010
22. Faschinger C, Mossböck G. Continuous 24 h monitoring of changes in intraocular pressure with the wireless contact lens sensor Triggerfish™. First results in patients. Der Ophthalmologe: Zeitschrift der Deutschen Ophthalmologischen Gesellschaft. 2010; 107(10):918–922. [PubMed: 20535482]
23. Koutsonas A, et al. Implantation of a Novel Telemetric Intraocular Pressure Sensor in Patients With Glaucoma (ARGOS Study): 1-Year Results Telemetric Intraocular Pressure Sensor. Invest Ophthalmol & Vis Sci. 2015; 56(2):1063–1069. [PubMed: 25613949]
24. Collins CC. Miniature passive pressure transensor for implanting in the eye. IEEE Trans Biomed Eng. 1967; 2:74–83.
25. Varel C, et al. A wireless intraocular pressure monitoring device with a solder-filled microchannel antenna. J Micromech Microeng. 2014; 24(4)
26. Chow EY, et al. A miniature-implantable RF-wireless active glaucoma intraocular pressure monitor. IEEE Trans Biomed Circuits Syst. 2010; 4(6):340–349. [PubMed: 23850751]
27. Chen PJ, et al. Wireless intraocular pressure sensing using micro-fabricated minimally invasive flexible-coiled LC sensor implant. J Microelectromech S. 2010; 19(4):721–734.
28. Araci IE, et al. An implantable microfluidic device for self-monitoring of intraocular pressure. Nat Med. 2014; 20(9):1074–1078. [PubMed: 25150497]
29. Leonardi M, et al. Wireless contact lens sensor for intraocular pressure monitoring: assessment on enucleated pig eyes. Acta Ophthalmol. 2009; 87(4):433–437. [PubMed: 19016660]
30. Lee JO, et al. Biocompatible multifunctional black-silicon for implantable intraocular sensor. Adv Healthc Mater. 2017; 6(4)
31. Lee JO, et al. A microscale optical implant for continuous in-vivo monitoring of intraocular pressure. Microsys Nanoeng. accepted and in print.
32. Doborjeh MG, et al. A spiking neural network methodology and system for learning and comparative analysis of EEG data from healthy versus addiction treated versus addiction not treated subjects. IEEE Trans Biomed Eng. 2016; 63(9):1830–1841. [PubMed: 26625401]
33. Osowski S, Linh TH. ECG beat recognition using fuzzy hybrid neural network. IEEE Trans Biomed Eng. 2001; 48(11):1265–1271. [PubMed: 11686625]
34. Antonietti A, et al. Spiking neural network with distributed plasticity reproduces cerebellar learning in eye blink conditioning paradigms. IEEE Trans Biomed Eng. 2016; 63(1):210–219. [PubMed: 26441441]
35. Zecchin C, et al. Neural network incorporating meal information improves accuracy of short-time prediction of glucose concentration. IEEE Trans Biomed Eng. 2012; 59(6):1550–1560. [PubMed: 22374344]
36. Petrenas A, et al. An echo state neural network for QRST cancellation during atrial fibrillation. IEEE Trans Biomed Eng. 2012; 59(10):2950–2957. [PubMed: 22929362]
37. Kamavuako EN, et al. Simultaneous and proportional force estimation in multiple degrees of freedom from intramuscular EMG. IEEE Trans Biomed Eng. 2012; 59(7):1804–1807. [PubMed: 22562724]
38. Hinton G, et al. Deep neural networks for acoustic modeling in speech recognition: The shared views of four research groups. IEEE Signal Proc Mag. 2012; 29(6):82–97.
39. Chen L, et al. Comparison of wavefront aberrations in rabbit and human eyes. Clin Exp Optom. 2014; 97(6):534–539. [PubMed: 25069625]

40. Herse PR, et al. Corneal edema recovery dynamics in the rabbit. A useful model? Invest Ophthalmol Vis Sci. 1990; 31(10):2003–2007. [PubMed: 2210996]

41. Kingma, DP., Ba, JL. ICLR. San Diego, CA, USA: 2015. Adam: A Method for Stochastic Optimization. Available: arXiv:1412.6980[cs.Lg]

42. Tranos P, et al. Postoperative intraocular pressure spikes: the need to treat. Eye. 2004; 18(7):673–679. [PubMed: 15002028]

43. Cooper RL, et al. Continuous monitoring of intraocular pressure: effect of central venous pressure, respiration, and eye movements on continual recordings of intraocular pressure in the rabbit, dog, and man. Br J Opthalmol. 1979; 63(12):799–804.

44. Buchacra LC, et al. Does Breath Holding Influence IOP Measurements? Invest Ophthalmol Vis Sci. 2009; 50(13):2872.

45. Hoffmann EM, et al. Intraocular pressure and ocular pulse amplitude using dynamic contour tonometry and contact lens tonometry. BMC Ophthalmol. 2004; 4(1):4. [PubMed: 15038831]

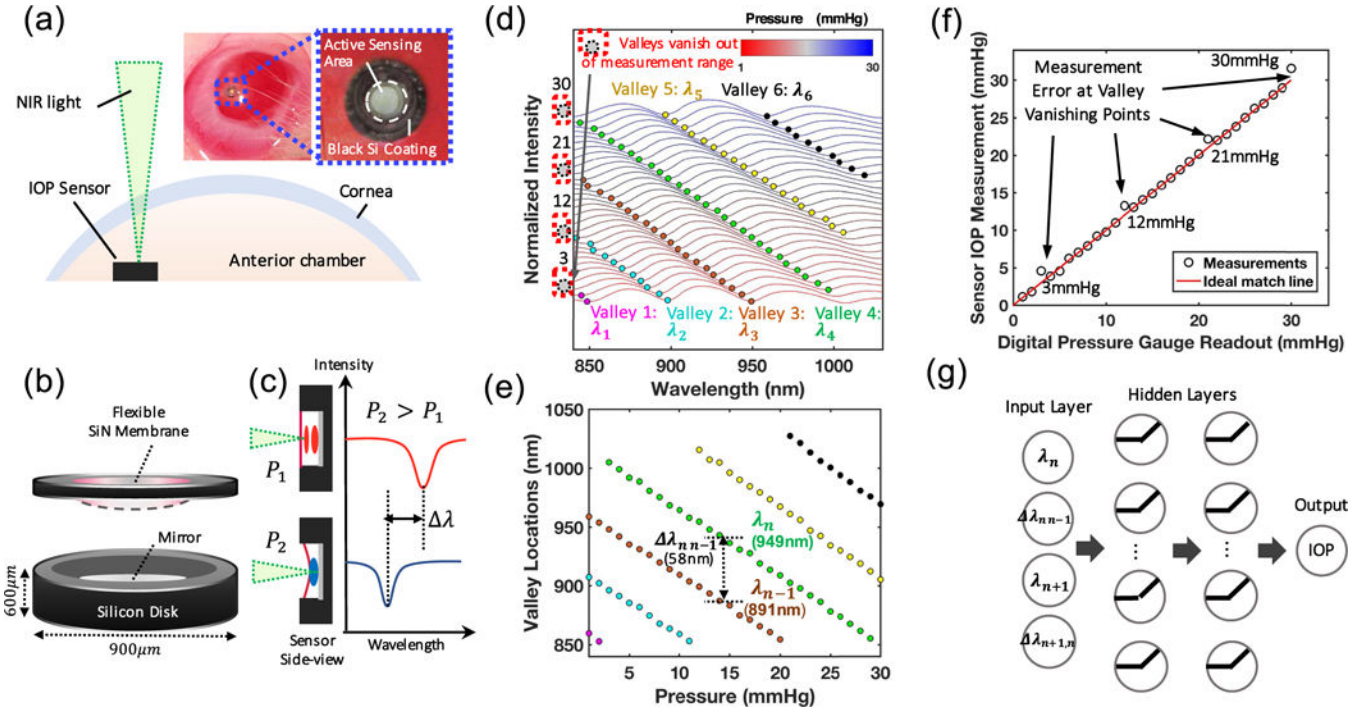

Fig. 1.

Light-probed IOP sensor and working principle of the ANN-basd SDA. **(a).** A simplified cross-sectional diagram and real image of the IOP sensor implanted in the anterior chamber. **(b).** IOP sensor with a flexible SiN membrane on the top and a Si surface on the bottom. **(c)**. Resonance profile of the sensor varies with membrane deflection caused by ambient pressure change. **(d).** Experimentally obtained resonance spectra of the IOP sensor as the pressure is altered from 1 mmHg to 30 mmHg. **(e)**. A valley trace plot of the three leftmost valleys in the full 1–30-mmHg range. $\lambda_{\mathbf{n-1}}$ refers to the visible leftmost valley where n is a natural number equal to or larger than 2. $\Delta\lambda_{\mathbf{n,n-1}}$ indicates the spacing between the n_{th} valley and $(n-1)_{th}$ valley. **(f).** Sensor IOP readout when spectra are manually post-processed by stitching the valley traces in (e). Significant measurement errors occur at the valley vanishing points. **(g).** Conceptual diagram of the feedforward ANN, which takes the two leftmost valley locations and inter-valley spacing of the optical spectrum, marked in (e), as inputs to compute IOP. Hidden layers are fully connected.

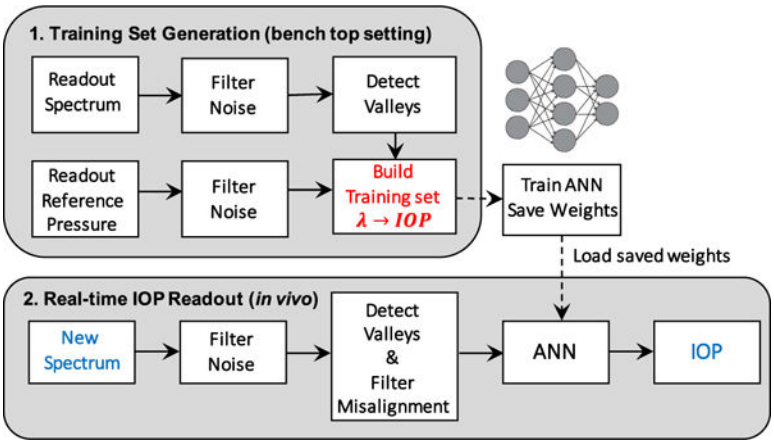

Fig. 2.

Flow diagram of ANN based signal demodulation. Applying the ANN is a two-stage process: (1) generating a training set in the benchtop testing (top); and (2) loading the trained ANN for real-time signal demodulation during *in vivo* experiments (bottom).

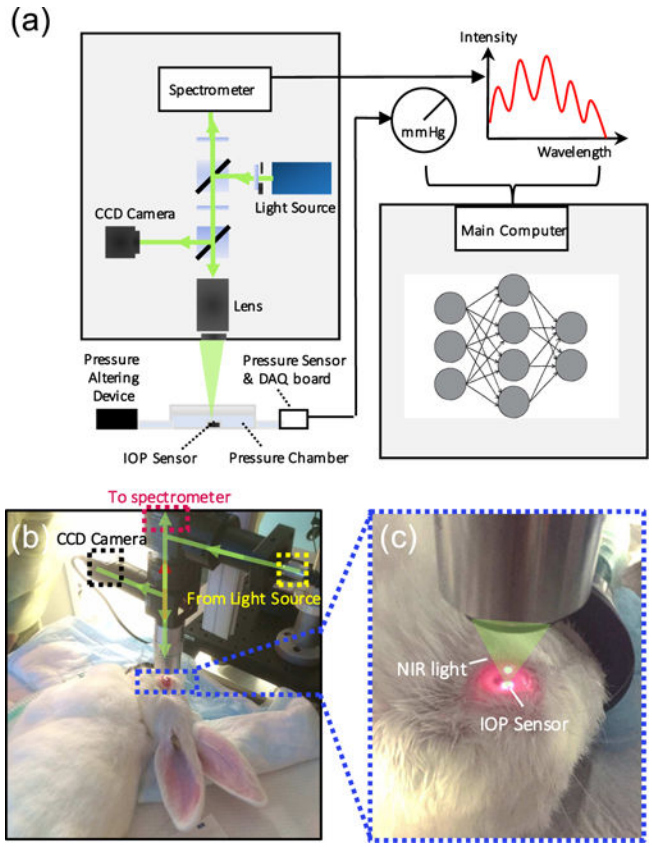

Fig. 3.

Optical bench-top and *in vivo* IOP measurement set-up. (**a).** An illustration of the bench-top measurement set-up (left). Optical spectra and its corresponding pressure values are extracted for ANN training (right). **(b).** *In vivo* measurement scene involving a rabbit under anesthesia undergoing spectrum measurements. Trained ANN from (a) is applied for real-time IOP readout. Measurements were performed using a detection set-up identical to the one in the left of Fig. 3(a). **(c)**. IOP sensor exposed to NIR region light.

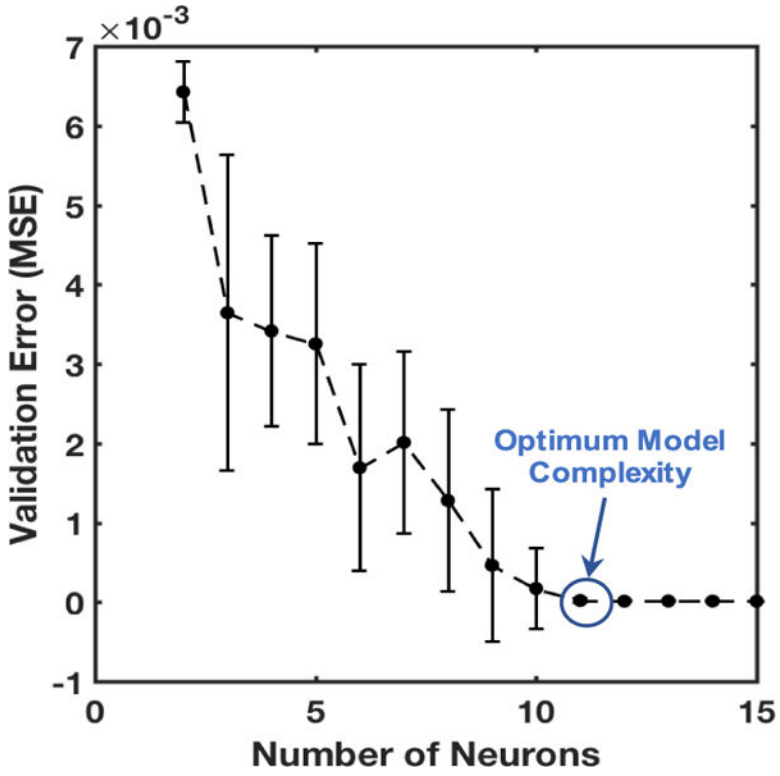

Fig. 4.

Optimization of the number of neurons in the ANN by comparing cross-validation error vs. the number of neurons. The error remains at the minimum level for 11 or more neurons, hence 11 neurons were chosen to minimize the computational load while achieving the minimum error.

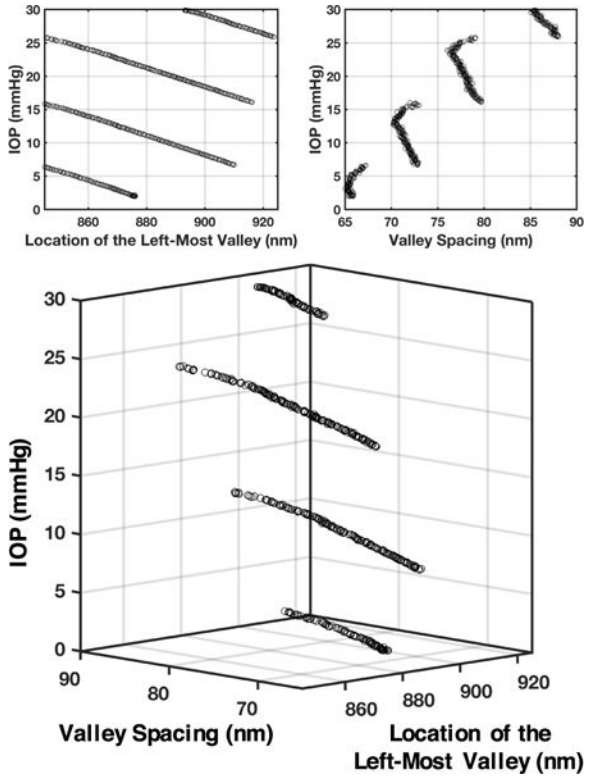

Fig. 5.

Inputs to the ANN for IOP mapping. Each IOP value generates a unique combination of a leftmost-valley location and a valley spacing, which is used to train the ANN and retrieve the original IOP value. Discontinuity in the 3D plot originates from the leftmost valley moving out of the spectrometer's measurement window due to pressure increase, which is illustrated in Fig. 1(d). The top-left graph is a 2D projection of the 3D plot showing IOP vs left-most valley location while the top-right graph is a 2D projection of the 3D plot showing IOP vs inter-valley spacing. Both 2D graphs help visualize that the input-feature set provides a complete coverage of the IOP range from 0 to 30 mmHg.

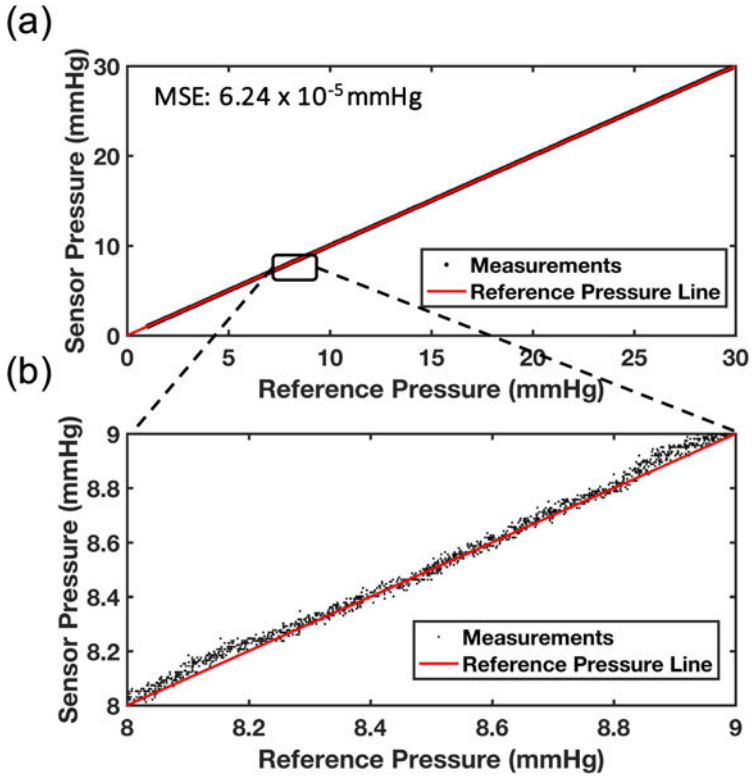

Fig. 6.

IOP-readout accuracy of the ANN-based SDA for the physiologically observed IOP range (0–30 mmHg) characterized in the pressure-controlled chamber. **(a).** Comparison between the measurements (black dots) and the reference pressure line (red line). **(b).** A zoomed-in view of the plot shown in (a) between 8 and 9 mmHg. The results showed excellent matching between measurements and the reference pressure line, with deviations less than ±0.1 mmHg.

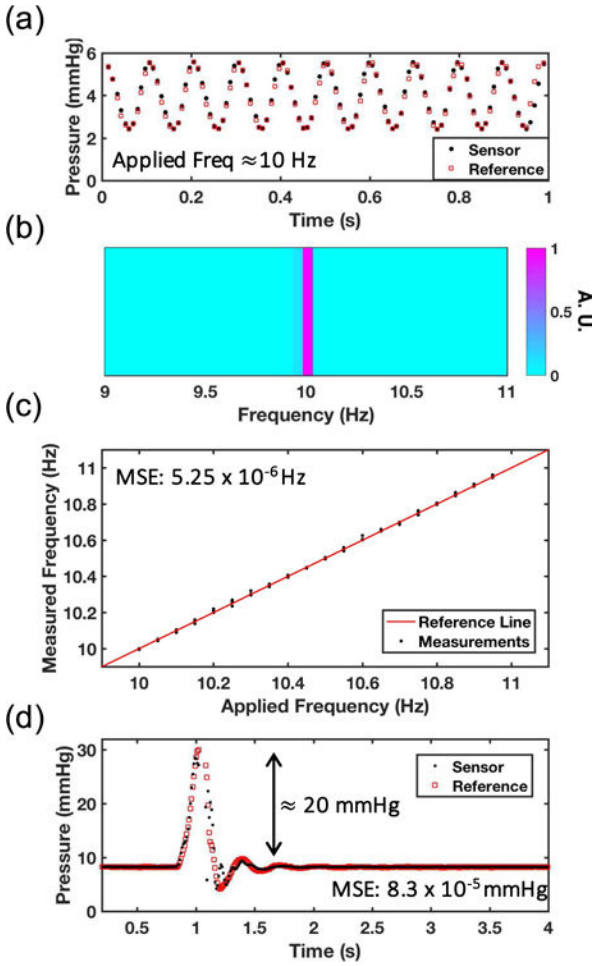

Fig. 7.

Temporal resolution of the IOP readout measured using the bench top testing setup made of a pressure-controlled chamber and a sinusoidally-varying and pulsating pneumatic source. **(a).** Close agreement between the ANN-produced pressure (black dots) levels and the reference pressure readings (red squares) from a digital gauge during a 10-Hz sinusoidal variation in pressure. **(b).** FFT of the IOP readout produced by the ANN-integrated sensor shown in Fig. 7(a), with a clear peak at 10 Hz as expected. **(c).** Comparison between the IOP-sensor-measured frequency and applied frequency. It shows a very close match over the frequency range of 10 and 11 Hz, which is well below the Nyquist frequency of our IOP system sampling at 100 Hz. **(d).** Comparison between the IOP-sensor readout (black dots) with the reference pressure values obtained using a digital pressure gauge (red squares) during a 20-mmHg pressure spike with the full width at half maximum of 0.4 s.

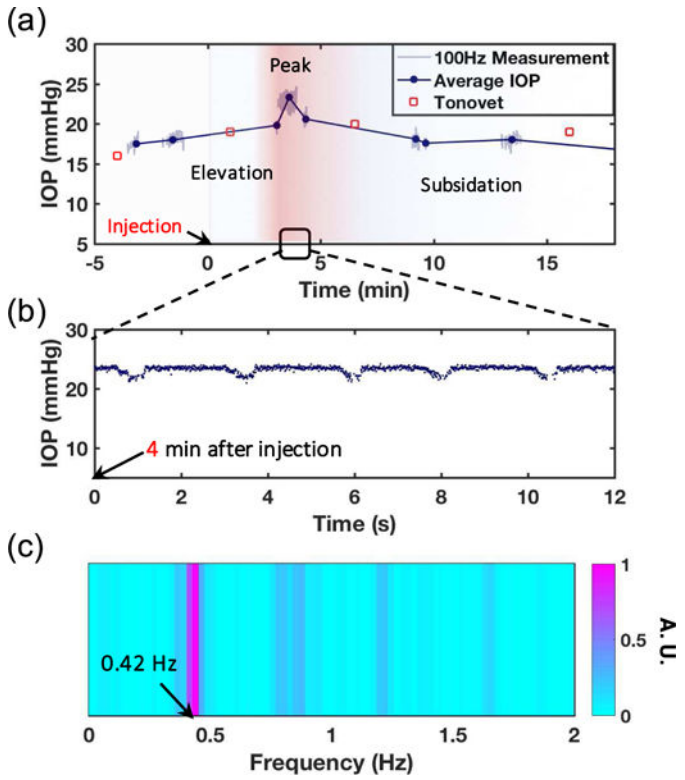

Fig. 8. In vivo

IOP measurements in live rabbits.**(a).** Transient IOP elevation induced by intravitreal injection carried out at time = 0. **(b)**. 12 seconds of high-temporal-resolution IOP measurements showing periodic dips in IOP. This is obtained during the peak IOP elevation around t = 4 min in Fig. 8(a). Time = 0 in this graph corresponds to time = 4 min in the previous plot shown in Fig. 8(a). **(c)**. FFT spectrum of peak IOP.

TABLE I

Summary of IOP Sensing Technologies

IOP Sensor Device/Method	Device/Method Type	Device Size	Accuracy/Sensitivity	Meas. Rate (Hz)	*In Vivo* Meas.? (Meas. Dist.)
DCT [18]	Tonometry	n/a	±1 mmHg	100	Yes (0 cm)
Capacitive Sensor [20]	Contact Lens	π×7×7×0.1 mm^3	200 ppm/mmHg	Discrete	No
Telemetric Sensor [26]	Implant	3×6×0.3 mm^3 27 mm antenna	±1.3 mmHg	Discrete	No
Wireless LC Sensor [27]	Implant	π ×2×2×l mm^3	±2.5 mmHg	Discrete	No
Microfluidic Sensor [28]	Implant	0.5×2×0.3 mm^3	±0.5 mmHg	Discrete	No
Sensimed TriggerFish [29]	Contact Lens	π ×7.05×7.05×0.6 mm^3	0.07 mV/mmHg	10	Yes (0.5 cm)
Optomechanical Sensor (Ours)	**Implant**	**π×0.45×0.45×0.6 mm^3**	**±0.1 mmHg**	**100**	**Yes (12 cm)**

IEEE Sens J. Author manuscript; available in PMC 2018 October 05.